Fatigue Crack Propagation in Friction Stir Welded Aluminium Alloy 5083

Nikita Kaminskyy

nikita.kaminskyy@tecnico.ulisboa.pt

Instituto Superior Técnico, Universidade de Lisboa, Lisboa, Portugal

January 2021

Abstract

Fuel economy and weight reduction are among key challenges currently faced by the aerospace industry. In an already highly regulated field, where every technology must be proven before it is approved, overcoming these without compromising the safety and performance of the next generation of air and space vehicles is a top priority when it comes to employing new joining techniques and evaluating its performance in operating conditions. Ergo, this study tackles a common problem responsible for a great part of failures in engineering structures subjected to cyclic loading conditions, fatigue. In particular, this investigation focuses on Fatigue Crack Propagation (FCP) in two non heat-treatable aluminium alloy sheets joined with an innovative solid-state joining method dubbed Friction Stir Welding (FSW). Building on the existent work available on this matter, a multi-subject investigation was performed on the FSWed butt joint to assess its behaviour when subjected to FCP. The research included an in-depth material characterization, and evaluation, where tensile tests paired with Digital Image Correlation (DIC) for strain field measurements, microstructure and microhardness analysis, as well as surface roughness measurements were done. Additionally, a numerical study of FCP was developed within a Computer-Aided Engineering (CAE) software with the help of the eXtended Finite Element Method (XFEM). Among the obtained data, the mechanical performance of the joint revealed inconsistent results mostly due to the existence of the Kissing Bond (KB) defect found during microstructure analysis. The numerical analysis demonstrated promising capability in complementing or even replacing the experimental studies as long as correctly modelled into the software.

Keywords: Friction Stir Welding, Fatigue Crack Propagation, XFEM, Non-Heat Treatable Aluminium Alloy

1. Introduction

The increase in air traffic foreseen for the following decades caused a need in the aerospace sector to rethink its strategy when it comes to developing new vehicles, prioritizing measures that lower environmental impact in order to combat one of the biggest problems faced in the current century, the climate change. One such measure is the weight reduction of structures associated with fuel economy which consequently opened the door for the introduction to innovative joining techniques such as Friction Stir Welding (FSW).

With FSW reaching the early stage of commercial use, joining the material that makes up to 75% - 80% of a modern aircraft without the use of additional mechanical components became a promising solution to the given problem.

Just as any other novel technology it does not come without its drawbacks, and in an industry where safety and reliability are a top priority, a considerable amount of research and development must be done in a multitude of subjects, prior to any attempt in implementing and consequently certifying it.

One of the subjects being exhaustively studied in FSWed metal alloys is Fatigue Crack Propagation (FCP). Acknowledging the fact that fatigue is usually the dominant failure mode for components in service, especially for weldments, it is of utmost importance to have a good understanding of the performance of FSWed joints under cyclic loading conditions.

For those reasons, this study focuses on performing an in-depth investigation on FCP in FSWed non heat-treatable aluminium alloy in the form of a Compact Tension (CT) specimen, where a complete welding joint characterization is done in the beginning. Additionally, a numerical study is performed to complement the experimental part of this investigation.

2. Methodology

To develop the experimental procedure of this research, a series of specimens had to be designed and produced from two FSWed sheets of AA5083-H111. Prior to advancing with FCP tests, the joint had to be characterized through a set of experimental procedures among which microstructure and microhardness analysis, tensile tests, and surface roughness measurements.

The numerical analysis was developed in a commercially available Finite Element (FE) software, where a CT specimen was modelled within an elastic domain, with two distinct analyses being performed to the model.

2.1. Base material properties

The material used in this study was an aluminium alloy AA5083-H111, known for its exceptional performance in extreme conditions and the capacity to retain very good strength after welding. Its mechanical and chemical properties are displayed in Tables 1 and 2, respectively.

Parameter	Value
E (GPa)	70.3
σ_y (MPa)	161
σ_{UTS} (MPa)	302
Elongation (%)	20
ν	0.33

Table 1: Mechanical properties [6]

Element	Al	Mg	Mn	Fe	Cr
Weight (%)	bal.	5.26	1.02	0.19	0.15

Table 2: Chemical properties [6]

2.2. Specimen development

Two 300 x 100 mm sheets with a thickness of 5 mm have been previously FSWed in butt configuration using an *ESAB Legio FSW 3UL* numeric control equipment, with the welding parameters displayed in Table 3. The tool employed in the production had a 16 mm wide shoulder with threaded tapered pin profile on its end and it rotated in the clockwise direction.

All the specimens were designed according to the American Society for Testing and Materials (ASTM) E647 [1] and E8 [2] standards. In total, 6 of them were extracted from the sheets, using wire Electro Discharge Machining (EDM) - 3 CT specimen for FCP testing, 2 tensile specimens for strain field measurements using Digital Image Correlation (DIC) analysis and 1 metallographic sample to be used in microhardness and microstructure observations.

Parameter	Value
Axial force (kgf)	550
Rotation sp. (rpm)	1000
Traverse sp. (mm/min)	10
Plunge (mm)	4.3
Tilt (°)	0

Table 3: FSW parameters

2.3. Tensile tests

Tensile tests were conducted to determine *quasi-static* mechanical properties of the joint as well as to extract stress-strain curves from various characteristic weld zones, namely SZ and TMAZ, using 2D DIC. Both specimens, whose geometry is shown in Figure 1, were spray-painted a stochastic pattern on the surface where the weld line was located and tested on an *INSTRON 3369* universal testing system with 50 kN of maximum load capacity. The applied crosshead speed was 1 mm/min.
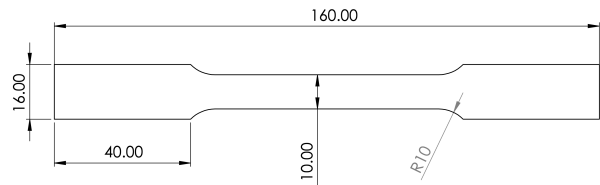

Figure 1: Tensile specimen with dimensions in mm

For image acquisition, one *Allied Vision Stingray F504B* high-performance camera paired with *Hedler DX15* lighting system was required. The image capture speed was set to 3 frames per second. Post-processing was done in *Correlated Solutions VIC-2D 2009* software.

2.4. Roughness measurements

Linear surface roughness of the welded joint area was determined prior to any machining or polishing of the specimen. A *Filmetrics Profilm 3D* optical profilometer, with a 20x objective, was used to analyze regions of interest.

The strategy behind roughness measurements consisted of taking 5 independent images, with a surface scanned area of 1.0 x 0.85 mm^2, along the weld line from three characteristic FSW zones - TMAZ+HAZ-AS, SZ, and TMAZ+HAZ-RS - making a total of fifteen scans, as illustrated in Figure 2 (a) (the red squares indicate the scan areas). In Figure 2 (b), (c), and (d), 3 examples of the characteristic surface morphology of different regions can be observed as 3D topographic images.

Linear roughness values were measured 6 times in each of 15 scans - 3 measurements along *x*-direction and another 3 measurements along *y*-direction - using a tool in *Profilm 3D* software named *Line Roughness*.
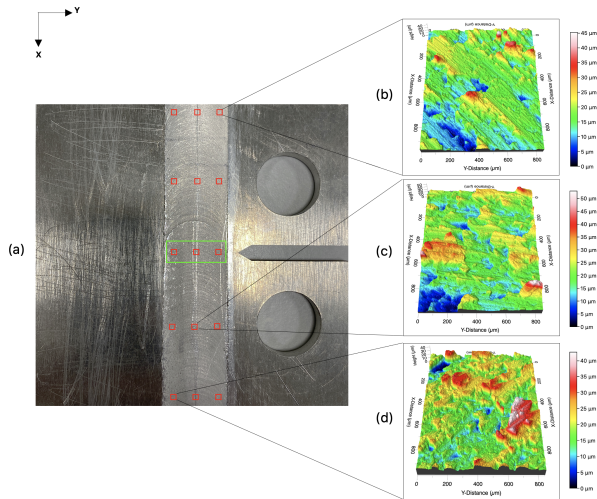
Figure 2: Photograph of the analyzed specimen with examples of the 3D characteristic surface morphology of (b) TMAZ+HAZ on AS, (c) SZ and (d) TMAZ+HAZ on RS

Additionally, an image of a bigger area across the entire joint width was taken, around the region of FCP. In order to form a topographic image with an approximate area of 17 x 5 mm^2, a total of 189 images of 1 x 0.85 mm^2, with a 20% of overlap, were obtained and stitched together.

2.5. Microstructure analysis

A 30 x 12 mm sample was embedded in a small cylindrical container within an epoxy mixture with a ratio of 25 : 3 parts of resin to hardener and left to cure for two days at an ambient temperature. Followed by several stages of grinding and polishing, being the last step a 1 μm diamond paste polish, the specimen was ready to be analyzed. An *Olympus CK40M* optical microscope paired with a digital camera was used in order to examine the areas with more detail.

2.6. Microhardness measurements

Vickers microhardness assessment was performed on the same sample that was used in the microscopic analysis and no additional preparation was done to the specimen. The tests were carried out on *Shimadzu HMV-2* microhardness tester with a load of 200 g and 10 seconds of force duration. A total of 117 measurements were made (39 measurements per line), at 1.0 mm (upper), 2.5 mm (middle), and 3.5 mm (lower) from the top of the sample. The middle 10 mm of the specimen were measured with an interval of 0.5 mm between each indentation and, outside of this area, all indentations were made with 1.0 mm between each other.

2.7. FCP Testing

FCP was the main topic of this study and required the production of 3 similar CT specimens as per ASTM E647 [1]. The dimensions of the specimens, illustrated in Figure 3, are dependent on the primary requirement given by the standard that is related to the crack size.

Crack is considered to be in the valid domain as long as Equation 1 is respected

$$(W - a) \geq \left(\frac{4}{\pi}\right) \cdot \left(\frac{K_{max}}{\sigma_y}\right)^2 \qquad (1)$$

where $(W - a)$ is the specimen's uncracked ligament, K_{max} is the maximum Stress Intensity Factor (SIF) and σ_y is Base Material's 0.2% offset yield strength. The load applied to the specimen was P_{max} = 4 kN, as it allowed for a satisfactory crack growth length of approximately 33 mm.
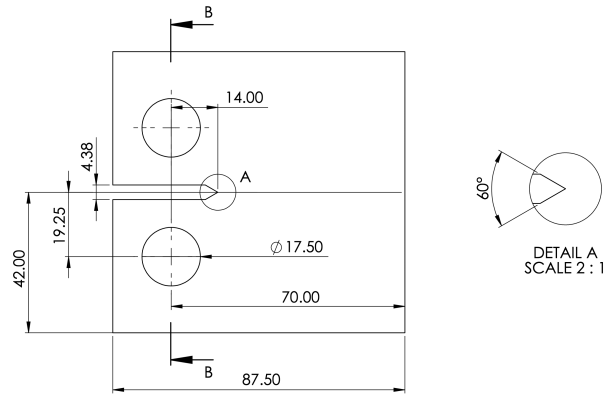

Figure 3: CT specimen with dimensions in mm

In order to be able to visualize crack propagating, all specimens were subjected to several treatment and machining processes, among which surface milling on both sides, grinding with five different wet sandpapers ranging from 300 to 4000 grit, and polishing with a fine paste, obtaining in the end a surface with mirror-like finish.

The FCP was evaluated on an *Instron 8502* servohydraulic fatigue testing system with a load cell rated at 10 kN for dynamic purposes. Monitoring of the cracks was done with the help of two USB digital microscopic cameras, *Dino-Lite Edge* and *Veho Discovery Deluxe*, paired with 2 LED lights, one for each side of the specimen. Both of them were mounted on purposely designed and fabricated 3D-printed supports and fixed onto vertical metallic rods installed close to the hydraulic pistons of the testing equipment. For the crack measurements, *Dino-Lite* and *Fiji* software were used. On each side of all three specimens, a real size 40 mm ruler was attached to serve as a calibration scale to the microscopic cameras.

2.8. Finite Element modelling

The FE model was developed in Abaqus, as close as possible to the experimental setup. Overall, two analyses were performed - a static one for

3

SIF evaluation and a dynamic one for FCP simulation. Both analyses were performed inside the elastic domain of the material (only E, σ_y and ν parameters were used) and the joint was not modelled due to lack of available data for each characteristic FSW region. In both cases, the geometry of the model was the same and only the mesh technique and the crack behaviour differed from one another. C3D8R elements were used in the global mesh, and C3D8 elements were used in the enriched areas of the model. The crack itself was modelled with the help of eXtended Finite Element Method (XFEM).

2.8.1 Static analysis

This analysis was performed for the purpose of validating the correct modelling of the specimen, by comparing the K_{max} obtained in Abaqus with the theoretical expression for K_{max} obtained from ASTM E647 [1] for the entire range of valid crack lengths.

$$\Delta K = \frac{\Delta P}{B \cdot \sqrt{W}} \cdot \frac{(2 + \alpha)}{(1 - \alpha)^{\frac{3}{2}}} \cdot (0.886 + 4.64\alpha -$$
$$13.32\alpha^2 + 14.72\alpha^3 - 5.6\alpha^4) \quad (2)$$

with $\alpha = a/W$ and $a/W > 0.2$. Equation 2 was manipulated by replacing ΔP with P_{max} = 4 kN in order to obtain K_{max}.

As for the meshing technique (see Figure 4), a small 1 x 1 mm^2 enriched area was defined at the crack front. The global mesh size was set to 1.5 mm per element while the local mesh size was defined after a convergence study was performed. The idea behind the convergence study was to fix the crack length at 15 mm (with crack growth disabled) and vary the number of elements in the previously defined enriched area and in through-thickness direction of the specimen, thus increasing the total number of elements in the mesh.
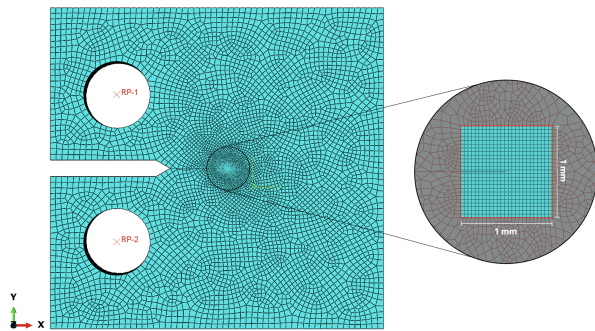

Figure 4: Model meshing for static analysis

A total of 13 simulations were performed for the convergence study (see Table 4) and the final configuration of the mesh was selected based on the

balance between the accuracy of the results and the time taken for the simulation to complete. K_I was calculated as a mean value of 5 contours around the crack tip in the central node.

X Y Z	Elements number	K_I (MPa·mm$^{1/2}$)	CPU Δt (s)
5 5 7	35343	758.96	14.5
10 10 7	42735	772.04	16.7
15 15 7	49602	772.48	22.3
5 5 10	50490	779.44	26.1
5 5 15	75735	745.94	97.1
10 10 15	91575	778.26	56.2
13 13 15	100065	777.96	63.5
16 16 15	109425	785.40	169.0
20 20 15	123645	781.40	86.8
25 25 15	125445	782.16	85.9
20 20 20	164860	783.36	380.5
20 20 25	206075	783.34	665.1
25 25 25	209075	787.16	697.6

Table 4: Mesh convergence for static analysis

2.8.2 Dynamic analysis

Dynamic analysis was performed in order to compare the experimental data with the numerical and observe how accurately is Abaqus able to simulate FCP. Unlike the static analysis, no concrete convergence study was done in this one, but rather some experimentation with the size of the elements and the proximity in the behaviour of FCP between them. The final mesh (see Figure 5) was defined with 2.0 mm per element in the global mesh, 0.5 mm per element in the enriched area and 6 elements in through-thickness direction, *i.e.*, 0.83 mm per element. Exactly as in the static analysis, C3D8R elements were used in the global mesh and C3D8 elements were used in an enriched area. The initial crack length was set to 5 mm in order to reduce the time of the simulation due to the initial uncertainty present in the model. Moreover, the crack growth behaviour was enabled and calculated based on fracture criteria given in Table 5.

Parameter	Value
c_1	0.001
c_2	0
c_3	4.337·10^{-6}
c_4	1.015
G_c	12.802
a_m, a_n, a_o	1

Table 5: Abaqus fracture criterion
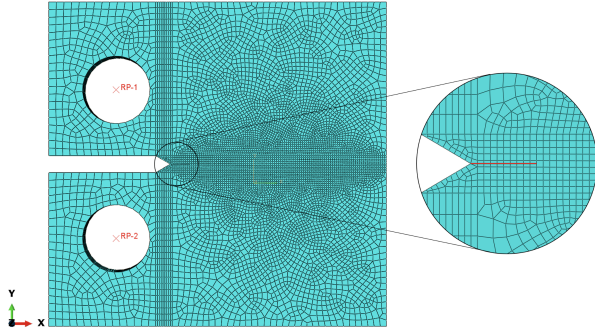
Figure 5: Model meshing for dynamic analysis

Figure 6: Stress-strain curves for specimen 1

The load was set as P_{max} = 4 kN and applied in the form of a periodic wave, given by Equation 3, with a frequency of 1 Hz and R = 0.1, to simulate the exact conditions of the experimental FCP

$$x = A_0 + A_1 \cos{(t - t_0)} + B_1 \sin{(\omega(t - t_0))} \quad (3)$$

with $A_0 = 0.55$, $A_1 = 0$, $B_1 = 0.45$, $t = -0.25$ and $\omega = 2\pi$.

Paris law constants, C and m, as well as fracture toughness K_{IC} used for the definition of fracture criterion of the model are given in Table 6.

K_{Ic} (MPa·mm$^{1/2}$)	C (mm/cycle; MPa·mm$^{1/2}$)	m
948.68	5.218·10^{-11}	2.03

Table 6: AA5083-H111 experimental parameters [5]

3. Results

This section presents all the relevant results withdrawn from the experimental and numerical analysis in the course of this investigation.

3.1. Tensile tests

Stress-strain curves were obtained for both tensile specimens (see Figures 6 and 7) from 3 different FSW regions and 1 from an entire strain field to serve as a reference. Specimen 1 showed greater tensile behaviour than specimen 2 by obtaining greater maximum stress and strain values. Nevertheless, mechanical properties of the joint deteriorated with reduction of both σ_y and σ_{UTS}, due to the heat generated during welding, hence causing the material to behave differently. SZ demonstrated lower ductility than TMAZ RS, while TMAZ AS revealed inconsistent results.
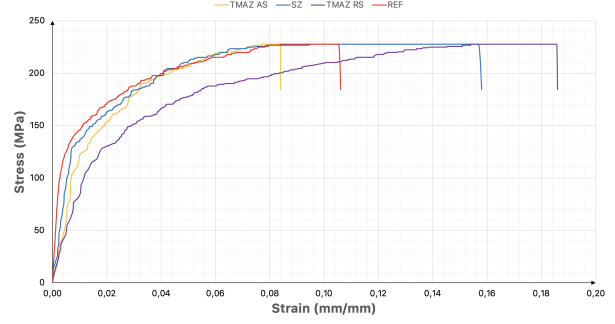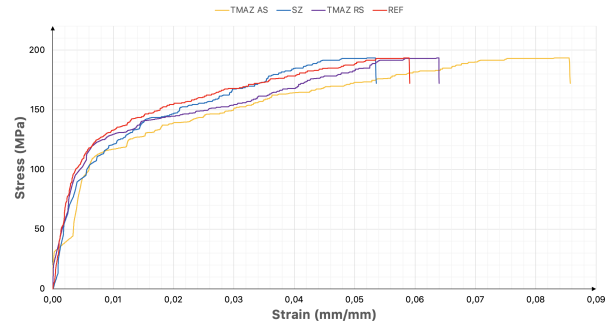

Figure 7: Stress-strain curves for specimen 2

Load-displacement curves (see Figure 8) were also extracted for both specimens. Specimen 1 fractured sooner than specimen 2, thus showing a difference of 34.2 MPa in σ_{UTS}, and a weld efficiency of 76% and 64%, respectively. Maximum values for each curve are given in Table 7. Additionally, both specimens showed a similar rupture pattern (see Figure 9), between SZ and TMAZ AS, and identical to the KB defect found during microstructure analysis.
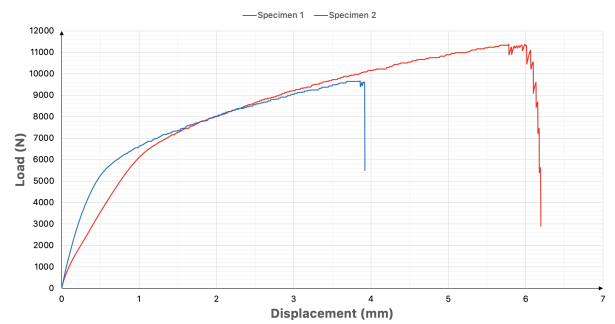

Figure 8: Load-displacement of tensile specimens

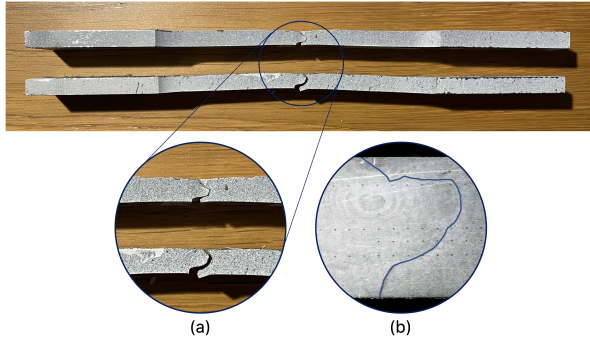| Specimen	Max. load (kN)	Max. disp. (mm)	σ_{UTS} (MPa)
1	11.38	6.20	227.70
2	9.67	3.92	193.50

Table 7: Maximum load-displacement values

5

Figure 9: (a) Close-up of tensile specimen failure compared with (b) a microscopical image of the cross-sectional area with KB defect represented by a dark blue line

Figure 10: Microhardness profiles and a microscopic image of the analyzed samples crossection

3.2. Microstructure analysis

The microscopic analysis allowed for the different regions to be observed. Although the macroscopic observations did not reveal any visible defect, under the microscope KB defect could be identified between SZ and TMAZ AS. This phenomenon is common in FSW and is usually caused by the insufficient penetration of the tool pin into the workpiece material, causing incomplete welding. Another cause is the presence of a native, protective oxide on the surface of aluminium alloys, that if not sufficiently broken up during the FSW, weakens the bond strength [4].

3.3. Microhardness measurements

Microhardness measurements were performed on the same sample used in the microstructure analysis. In Figure 10 are represented profiles from 3 different measuring lines taken across the thickness of the specimen, symbolically marked with the dotted lines.

The highest values were observed in SZ indicating that dynamic recrystallisation occurred in that area and finer grains were formed. However, the upper profile showed a dip in the same area with values very close to ones of BM - this can be explained by the proximity to the top of the weld where the tool softens the material more due to higher temperatures being generated during FSW.

TMAZ showed an accentuated decrease in hardness values the center increased due to the coarsening of the hardening phase. HAZ hardness values did not appear to suffer any effect from the heat, presenting values very similar to ones found outside the welding width.
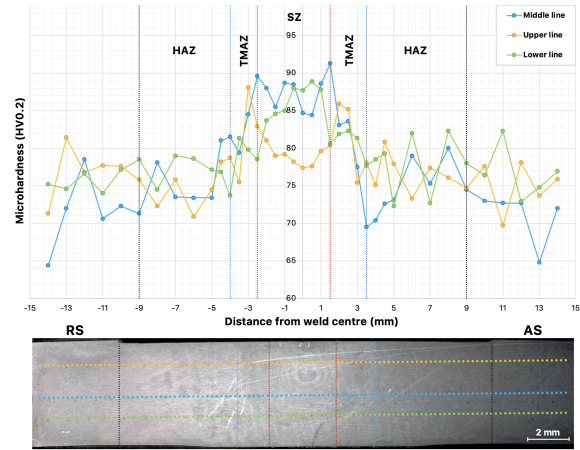
3.4. Surface roughness measurements

From a total of 90 measurements taken, an average R_a was calculated for each of the 3 FSW regions of the joint. According to the literature [3], the results (see Table 8) are in line with what was expected, with the SZ presenting the lowest value.

	TMAZ + HAZ AS	SZ	TMAZ + HAZ RS
Total Mean Value	1.016	0.914	1.113

Table 8: Obtained R_a measurements. Units are in μm

The stitched 3D image of the joint width (see Figure 11) revealed the circular marks left by the tool during welding and a central line that was made on purpose by a caliper, to serve as a guideline during the process of the specimen manufacture. The 2D profile across the entire weld (see Figure) reveals the existence of a "valley" in the central part of the weld with an approximate depth of 20 - 30 μm. A probable cause for the formation of the given "valley" is the fact that during the stirring process the tool pushes some of the material to the edges of the welding line. This depth is consistent with the volume of material that had to be removed during specimen preparation, with mechanisms such as surface milling, grinding, and polishing, resulting in a final sample thickness of roughly 4.5 mm.
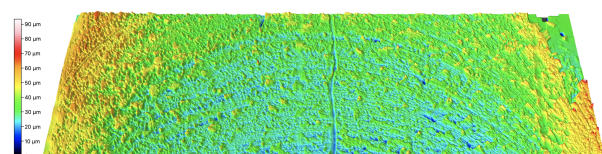

Figure 11: Optical profilometry image showing surface morphology of a 17 x 5 mm^2 area across the weld
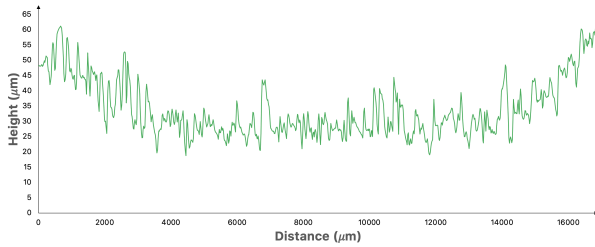
Figure 12: Linear profile of the surface represented in Figure 11

3.5. Experimental FCP

FCP tests were severely limited due to faulty fatigue testing equipment and only 2 out of 3 specimens were tested. The initial load was set to be P_{max} = 3 kN as it allowed for the entire joint to be covered by the valid crack domain. This scenario was applied to specimen 1, after opening a pre-crack with an approximate length of 1 mm, using P_{max} = 4 kN and R = 0.1 within 4000 cycles. The tests proceeded as planned and after 655897 cycles applied to the specimen with P_{max} = 3 kN, the crack had grown 0.5 mm, leading to believe that the pre-crack was not opened in the beginning. A decision was made to ramp up P_{max}, and consider that every cycle and load applied to date served to open a pre-crack with a length between 1.37 and 1.56 mm, depending on the side.
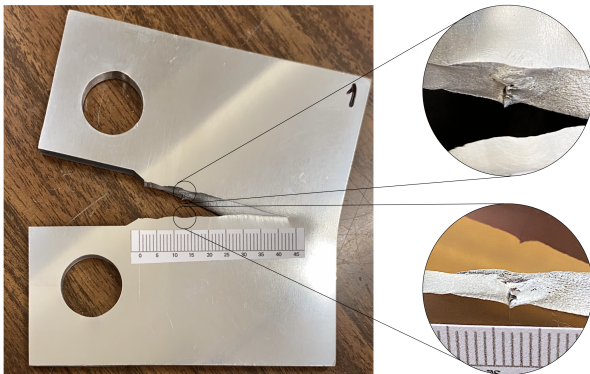

Figure 13: CT specimen with apparent defects in the welded joint

After resetting the cycle counters, P_{max} = 5 kN, R = 0.1, and a maximum frequency f = 4 Hz, were applied to the same specimen. Rapid crack growth was observed from the beginning, with the crack reaching a little over 5 mm in length after 70000 cycles. The total fracture of the specimen was observed after 93210 cycles. This sudden and uncontrolled crack growth can be explained by the possible existence of microscopic cracks provoked by the previous tests with P_{max} = 3 kN, which could not be observed with the available equipment. Another plausible explanation is the existence of voids and imperfections, such as the already detected

KB, in the FSW joint itself. Figure 13 depicts the fractured specimen with the top and bottom of the crack zoomed-in, where the defects can be observed. The location of the defect is coincident with the location of the previously found KB and with the region where both sheets of aluminium alloy meet.

For those unfortunate reasons, specimen 1 only allowed for 3 data points to be collected during experimental procedures (see Figures 14 and 15).
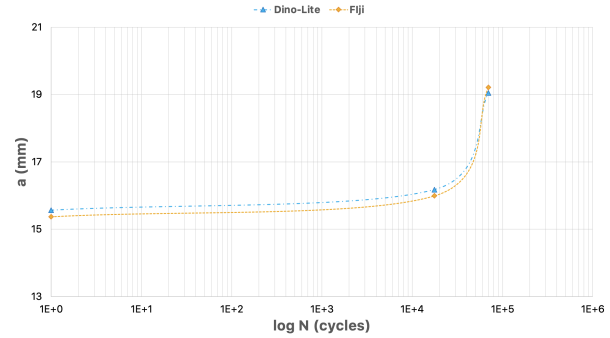

Figure 14: Crack growth with P_{max} = 5 kN. Each color represents each side of the specimen and the software used to measure the crack length
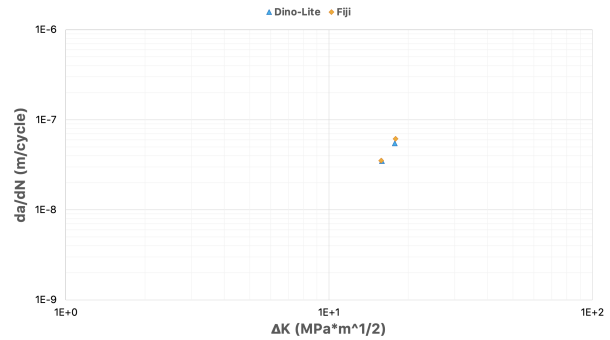

Figure 15: FCP curve for P_{max} = 5 kN

Concerning specimen 2 and with the lessons learned from specimen 1, it was decided to test the following specimens with reduced load P_{max} = 4 kN. Not only this cutback would allow covering a greater width of the joint when compared to P_{max} = 5kN, but also to slow down the rate of FCP. To ensure the opening of the pre-crack, P_{max} = 6 kN and R = 0.1 was applied to this specimen during 2036 cycles with f = 3 Hz, resulting in an approximate opening ranged between 1.06 and 1.55 mm, depending on the side where it was measured. The tests followed with P_{max} = 4 kN, R = 0.1, and f = 4 Hz, up until the failure of the fatigue testing equipment, making it impossible to continue with the experimental FCP. After 170316 cycles, the crack presented a length that ranged between 2.12 and 2.39 mm. In Figures 16 and 17 can be observed

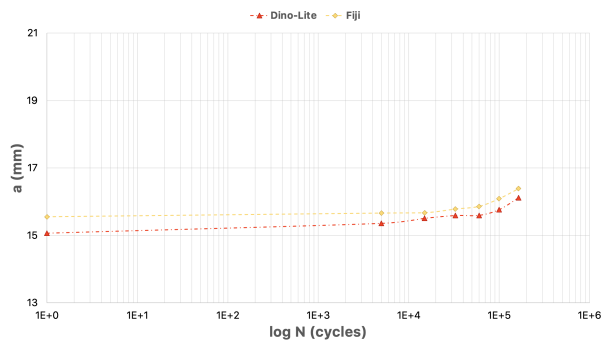a graphical representation of the collected data for specimen 2.

Figure 16: Crack growth with P_max = 4 kN. Each color represents each side of the specimen and the software used to measure the crack length
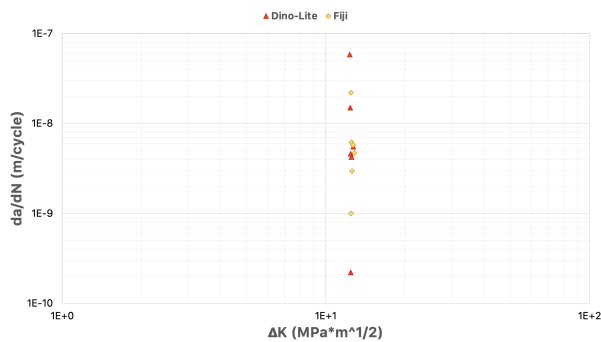

Figure 17: FCP curve for P_max = 4 kN

3.6. Numerical results
3.6.1 Static analysis

The purpose of the static analysis was to evaluate the accuracy of the model due to the fact of Abaqus being unable to determine SIF while simulating FCP. K_I was calculated by Abaqus for the entire valid crack length domain, *i.e.*, in the interval between a = 15 mm and a = 33 mm. The number of elements varied between 96030 and 136245.

It was possible to observe (see Figure 18) that, despite the difference in magnitude, both curves show a similar trend, with the error decreasing down to a little over 7 % when the crack size increases. A greater error, in the beginning, can be attributed to the poor meshing around the notch area, resulting in an overall smaller amount of elements in the model, thus lower accuracy. Another possible explanation for this deviation may lay in the difference of the shape factor Y definition. While in the standard, the shape factor is given based on an extensive experimental database of the same geometry, in Abaqus the shape factor must be calculated based on another more broad expression valid for a range of different geometries.
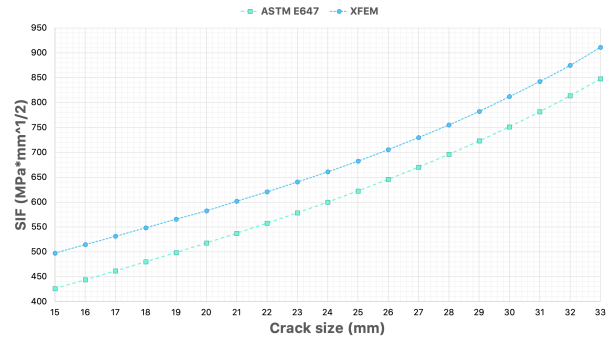

Figure 18: SIF estimation for XFEM model validation

From Figure 19 it was possible to observe the through-thickness effect found at the crack tip, which may be another responsible for the deviation in the magnitude of SIF. This complex mechanism is observed in 3D models, where SIF is not constant at all nodes across the thickness of the specimen. Maximum values of SIF are observed in the central nodes of the specimen with a decreasing behaviour of the calculated parameter towards the surface. The dashed line represents the theoretical value calculated for the same crack length according to the standard that is considered to be constant along the entire thickness of the specimen.
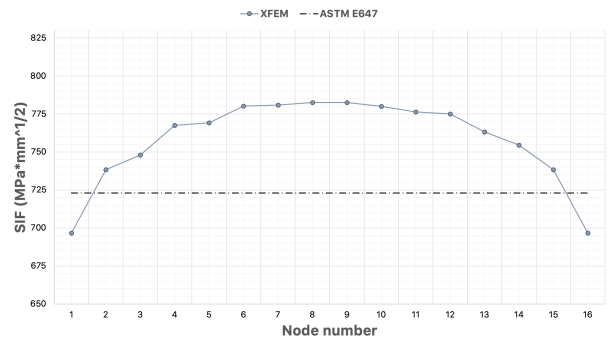

Figure 19: Comparison of SIF distribution across the thickness of the model, a = 29 mm

3.6.2 Dynamic analysis

Unlike initially planned, the results of this analysis were not compared with the experimental FCP due to lack of obtained data, but rather with the theoretical predictions given by Paris law.

For that matter, a final mesh with 47616 elements was generated with the majority of them being present in the enriched area for an accurate crack growth prediction. During the simulation, FCP happened perpendicular to the load applied by splitting the element into two parts, as expected. In the end, the number of load cycles was precisely noted for every cracked element as the fatigue crack propagated over time, resulting in the last value inside the valid crack domain, *i.e.*, a = 33

mm, being achieved after 685189 cycles on one side and 752113 cycles on the other.

The discrepancy between both values is attributed to the way the FCP happens within the software. Two fracture mechanisms were observed during the simulation (see Figure 20) - an initial one characterized by a *regular* FCP mechanism in through-thickness direction, and an *uncontrolled* one with an irregular fashion after a certain crack length is achieved. The irregular behaviour was observed when the crack propagation changed its direction and intersected the boundary between the elements, thus forcing the calculation to become more complex.
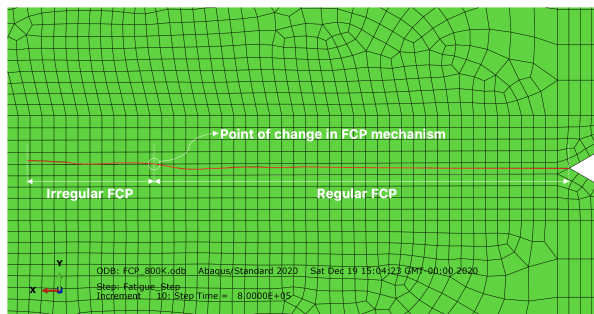

Figure 20: Representation of FCP mechanisms in Abaqus

Moreover, in Figure 21 is depicted a 3D image of the crack itself where it is possible to observe FCP behaviour through the thickness of the specimen and an approximate location of the point of change in the FCP mechanism.
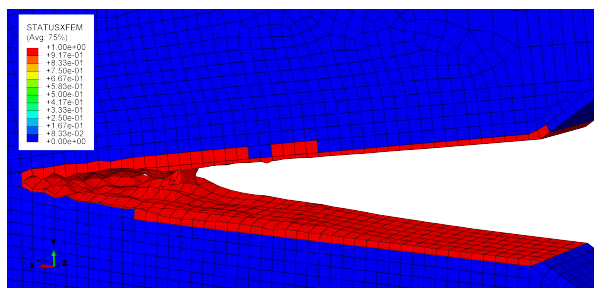

Figure 21: 3D image of FCP through the thickness of the specimen

As for the results, these were plotted in the common form in Figures 22 and 23. Overall, the results were found to be similar to what was expected from theoretical equations given by Paris law. The FCP rate represented in Figure 23 showed a good agreement between the points extracted from Abaqus and the Paris law prediction. Greater dispersion of the extracted points can be observed on the right-hand side of the plot, symbolizing the change in the FCP mechanism.
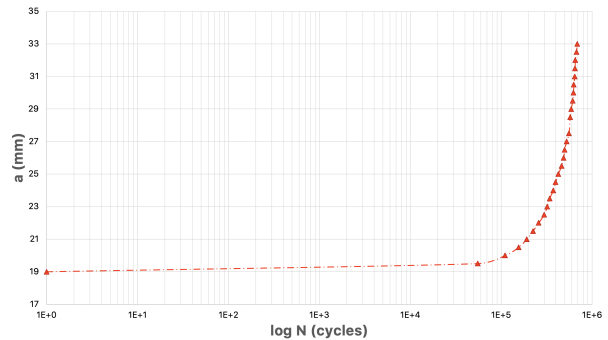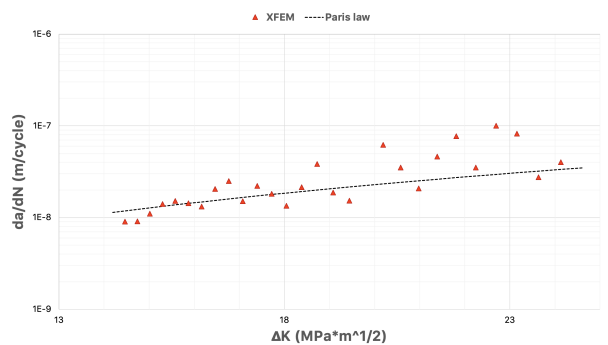

Figure 22: FCP behaviour in XFEM

Figure 23: Graphical comparison of FCP rate between data withdrawn from XFEM and Paris law

4. Conclusions

To begin with, microstructure and microhardness analysis helped to define and limit welding regions, information that was taken into account in all phases of this study. Additionally, microstructure analysis unveiled the expected behaviour resulting from the FSW process, where grain refinement in SZ impacted positively the mechanical properties of the material, later confirmed by microhardness tests. Moreover, microstructural observations allowed to detect a common butt joint defect, KB, which at the same time promoted mechanical and fatigue degradation of the piece, confirmed during tensile tests. The roughness of the joint surface allowed to observe the formation of a *valley* in the central part of the weld width.

Due to a combination of limiting factors in the course of this investigation, the amount of data collected during experimental FCP did not allow for an in-depth overview and conclusions to be written.

Concerning numerical results, Abaqus revealed very promising results when the object is correctly modelled into the software and the BC are accurately defined. Even with a limited amount of computer power, the SIF and FCP calculations revealed reliable results with reduced deviations when compared to their theoretical predictions. Overall, numerical studies of FCP not only can deliver viable results but also bring economical benefits by saving resources and time on performing

experimental studies.

As for future work, several recommendations can be done regarding the development of future researches.

With the aim of achieving a detailed study of FCP rate across characteristic FSW regions, a defect-free FSW joint must be obtained in the first place, either by doing a parametric study or by using an optimal set of parameters for a given material from the literature. Also, using a material with different mechanical properties that would allow for a greater load to be applied without sacrificing the valid domain of the crack length.

Another recommendation for future work would be to simulate the FCP in an elasto-plastic environment. A more detailed analysis would include the calculation of Paris constants for every FSWed region during experimental procedures and the FE modelling of the specimen with each region being assigned different fracture criteria in respect to the constants determined previously.

At last, it would be interesting to observe the influence of different parameters and configurations of the FE model, namely the difference in FCP for a range of stress ratios or to assess the behaviour of the crack in 2D and 3D models.

References

[1] Standard Test Method for Measurement of Fatigue Crack Growth Rates. Standard, ASTM International, West Conshohocken, PA, 2000.

[2] Standard Test Methods for Tension Testing of Metallic Materials. Standard, ASTM International, West Conshohocken, PA, 2013.

[3] R. K. Bhushan and D. Sharma. Investigation of mechanical properties and surface roughness of friction stir welded AA6061-T651. *International Journal of Mechanical and Materials Engineering*, 15, 06 2020.

[4] J. Schneider, P. Chen, and A. C. N. Jr. Formation of oxides in the interior of friction stir welds. 05 2016.

[5] A. R. Shahani, I. Shakeri, and C. D. Rans. Fatigue crack growth of Al 5083-H111 subjected to mixed-mode loading. *Journal of the Brazilian Society of Mechanical Sciences and Engineering*, 42, 08 2020.

[6] C. Vidal, V. Infante, and P. Vilaça. Fatigue behaviour at elevated temperature of friction stir channelling solid plates of AA5083-H111 aluminium alloy. *International Journal of Fatigue*, 62:85–92, 10 2014.